LANGMUIR Article
Cite This: Langmuir XXXX, XXX, XXX−XXX
pubs.acs.org/Langmuir

Wetting on Micropatterned Surfaces: Partial Penetration in the Cassie State and Wenzel Deviation Theoretically Explained

Chae Rohrs, Arash Azimi, and Ping He*

Department of Mechanical Engineering, Lamar University, Beaumont, Texas 77710, United States

Supporting Information

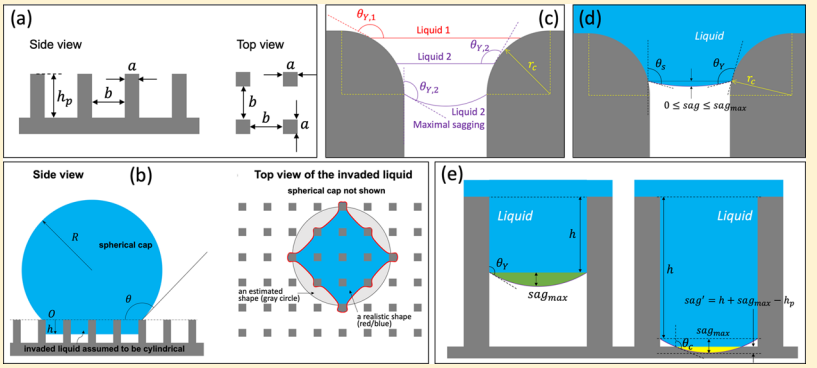

ABSTRACT: A liquid droplet on a micropatterned substrate equalizes into either the Cassie−Baxter (also called Cassie for short) or the Wenzel state. This paper investigates the wetting phenomena on ideal micropatterned surfaces consisting of straight micropillars at different pillar dimensions and spacings (the word "ideal" refers to being chemically homogeneous and free of submicron-scale roughness all over the micropatterned surface). Two modeling approaches are used: (1) a thermodynamic approach analyzing the Gibbs energy of the droplet−solid−gas system and (2) a computational fluid dynamics (CFD) approach studying the three-dimensional dynamic wetting process to validate the results of the first approach. The thermodynamic approach incorporates three creative submodels proposed in this paper: (i) a sagging model explaining the pillar edge effect, (ii) a touchdown model transitioning the droplet's partial penetrating condition toward its full penetrating condition, i.e., the Wenzel state, and (iii) a liquid-volume model dynamically computing the liquid volume between the pillar valleys while in the partial penetrating condition or in the Wenzel state. The results of the thermodynamic approach reveal (1) a small energy barrier between the Cassie and Wenzel states, (2) no partial penetration and sagging of the liquid in the Cassie state on the ideal straight micropillared surface, and (3) that the apparent contact angle in the most stable Wenzel state can be 5° or more lower than the prediction of the Wenzel equation when the pillar height is equal or greater than 75 μm. To the best of our knowledge, this paper presents the theoretical explanation of this Wenzel deviation on micropatterned surfaces for the first time in the literature. Utilizing the state-of-the-art continuum model developed by the authors in previous studies, the CFD approach investigates the same wetting conditions and confirms the same findings.

1. INTRODUCTION

Wetting phenomena on general rough surfaces have been thoroughly studied since the 1930s. Wenzel[1] proposed the famous Wenzel equation to predict the apparent contact angle of a liquid droplet on a rough surface

$$\cos\ \theta_{ap} = r\cos\theta_Y \tag{1}$$

where θ_{ap} is the apparent contact angle, r is the roughness ratio, and θ_Y is the Young's angle. Although Wenzel did not provide theoretical proof at that time, he presented a good number of experimental measurements to support his equation. Cassie and Baxter[2] proposed another equally famous equation, the Cassie−Baxter equation, to predict the apparent contact angle of a liquid droplet that sits on top of the microstructures of a porous surface

$$\cos\theta_{ap} = f\cos\theta_Y + f - 1 \tag{2}$$

where f is the area fraction of the liquid−gas interface occluded by the porous structures. Cassie and Baxter derived their equation through minimizing the total Gibbs energy and validated their model with experiments. These two great works revealed two distinct wetting states: (1) the Wenzel state, in which the liquid fully wets the rough structures, and (2) the Cassie−Baxter state, in which the liquid partially wets or sits on top of the rough structures. In the literature, the Cassie−Baxter state is often called the Cassie state for short.

Although the microfabrication technologies to create micropatterned surfaces, such as photolithography, soft

Received: September 24, 2019
Revised: October 28, 2019
Published: October 30, 2019

DOI: 10.1021/acs.langmuir.9b03002
Langmuir XXXX, XXX, XXX−XXX

lithography, and chemical etching, have been gradually developed since the late 1950s, the studies of wetting phenomena on micropatterned surfaces started as late as the 1990s.[3,4] Questions were raised for wetting on micropatterned surfaces. Will the Wenzel and Cassie−Baxter equations still be valid for micropatterned surfaces? Can both the Wenzel and Cassie states ever coexist on the same micropatterned surface? It is hypothesized that this will manifest in two variations: (1) If they are not coexisting in all conditions, then there will be a distinct boundary between the two states in terms of the micropattern configurations; or (2) if they are coexisting on certain micropatterns, there will be an energy barrier between the two states. To answer these questions, the thermodynamic approach using the Gibbs energy analysis is required. The Gibbs energy of the droplet−solid−gas system refers to the total surface energy of the liquid−gas, liquid−solid, and solid−gas interfaces.

Johnson and Dettre[5] analyzed the Gibbs energy of wetting on a rough surface with a specific roughness structure, whose contour was described as a function in cylindrical coordinates. Johnson and Dettre[5] formulated the total Gibbs energy considering the liquid volume between the rough structures; they solved the energy minimization iteratively using a computer program, reported the coexistence of the Wenzel and Cassie states together with multiple metastable states, and computed the energy barriers between any two neighboring states. Patankar[6] formulated the Gibbs energy for a liquid droplet on a micropatterned surface of straight micropillars neglecting the liquid volume between the micropatterns; he found that the solutions of the Wenzel and Cassie−Baxter equations were stable states; and he also compared the Gibbs energy between the two states. He, Patankar, and Lee[7] verified that the Wenzel and Cassie states would coexist on the same rough surface in certain conditions. Marmur,[8] using the same approach,[6,7] analyzed the Gibbs energy on a general rough surface with detailed derivations and went deep into the analysis of all local extrema. For the first time in the literature, Marmur's works "put the Wenzel and Cassie−Baxter equations into proper mathematical−thermodynamic perspective".[8] Patankar[9] applied Marmur's methodology of the local extrema analysis[8] to micropatterned surfaces with the additional consideration of gravity; Patankar[9] found that gravitational potential energy helped overcome the energy barrier, and that an energy barrier might not exist for some micropattern geometries. Furthermore, Tuteja et al.[10] explored the Gibbs energy of several micropattern geometries including straight pillars, saw shapes, spheres, and re-entrant textures. Whyman and Bormashenko[11] found that the Cassie-to-Wenzel transition was irreversible, i.e., the energy barrier from Wenzel to Cassie was much larger than that from Cassie to Wenzel.

Two types of the Cassie-to-Wenzel transition, i.e., depinning transition and sag transition, were explored using the Gibbs energy analysis.[12] Wetting transition on grooved surfaces has been studied with the Gibbs energy calculations on the incremental Cassie-to-Wenzel transition in one groove each time to find out the minimum energy path of transition.[13] The stability of the Cassie state on micropatterned surfaces were investigated using the energy analysis for two specific 2D and 3D pillared geometries.[14] A general differential equation of wettability with a set of coefficients for five micropatterns in both the Cassie and Wenzel states was derived based on the energy analysis.[15] A review paper on understanding wetting transition was published in 2015.[16] The micropattern geometry was studied to search the roughness contours that would make the Cassie state stable.[17] The changes of the Gibbs energy in the sagging process during the Cassie-to-Wenzel transition were analyzed on micropatterned surfaces made of circular straight pillars,[18,19] and the results showed that (1) the Gibbs energy gradient drives the transition, while the wetting force on the contact line resists the transition; (2) if the sagged liquid touches the substrate bottom, the Cassie-to-Wenzel transition would take place; (3) the transition becomes easier when either the pillar diameter and spacing increases (4) or the droplet volume increases; and (5) hierarchical structures will help inhibit the transition.[18,19] Using the Gibbs energy approach, wetting on double hierarchical micropatterned surfaces was studied and compared with experiments.[20]

Experiments found that the measured apparent contact angles could either be greater than both the Cassie−Baxter and Wenzel equations' predictions, or between the two.[21] The measured apparent contact angles in the Wenzel state were reported to be lower than the prediction of the Wenzel equation.[22] Theoretical analysis of the deviations from the Cassie−Baxter and Wenzel equations was discussed using reduced parameters.[23]

Besides the Gibbs energy studies, there are other modeling and simulation methods as well as experimental techniques to study the transition. The following is a brief summary of these experiments and simulations. Environmental scanning electron microscopy (ESEM) was used to take images of the contact line in the Cassie-to-Wenzel transition.[24,25] Using ESEM, the stability of the Cassie state on micropatterned surfaces was experimentally studied.[26] Acoustic waves were used to achieve Cassie-to-Wenzel as well as Wenzel-to-Cassie transitions on micropatterns.[27] The Cassie-to-Wenzel transition criteria has been proposed.[28] Dynamic effects such as impact and vibration were employed in transition experiments.[29] Wetting transition of ionic liquids has been studied in experiments.[30] Molecular dynamics has been used to study the coexistence of the Cassie and Wenzel states and their transition.[31] The lattice Boltzmann methods were used to compute the energy barriers between the Cassie and Wenzel states,[32] and to simulate a droplet transport technique utilizing the micropattern gradients.[33] The volume-of-fluid (VOF) method was used to investigate the effect of pillar height on the Cassie and Wenzel states at a prescribed local contact angle.[34] In prior works of the current authors, a slip boundary model was developed with experimental validations on flat and micropatterned surfaces; this model has been used in VOF simulations to capture static and dynamic contact angles consistent with experiments.[35,36]

This paper mainly focuses on the thermodynamic approach of wetting on micropatterned surfaces to theoretically elucidate the physical conditions of the Cassie and Wenzel states, i.e., (1) the degree of liquid sagging in the Cassie state, and (2) the effects of considering the liquid volume trapped between micropatterns in modeling. In addition, continuum simulations are used to support the findings from the Gibbs energy studies. The rest of the paper is organized as follows. Details of the thermodynamic modeling are presented in Section 2; the continuum modeling methods are briefed in Section 3; results and analysis are discussed in Section 4; and finally, Section 5 summarizes the conclusions.

2. THERMODYNAMICS OF WETTING

A liquid droplet on a micropatterned substrate equalizes into either the Cassie or the Wenzel state. Multiple metastable

DOI: 10.1021/acs.langmuir.9b03002
Langmuir XXXX, XXX, XXX−XXX

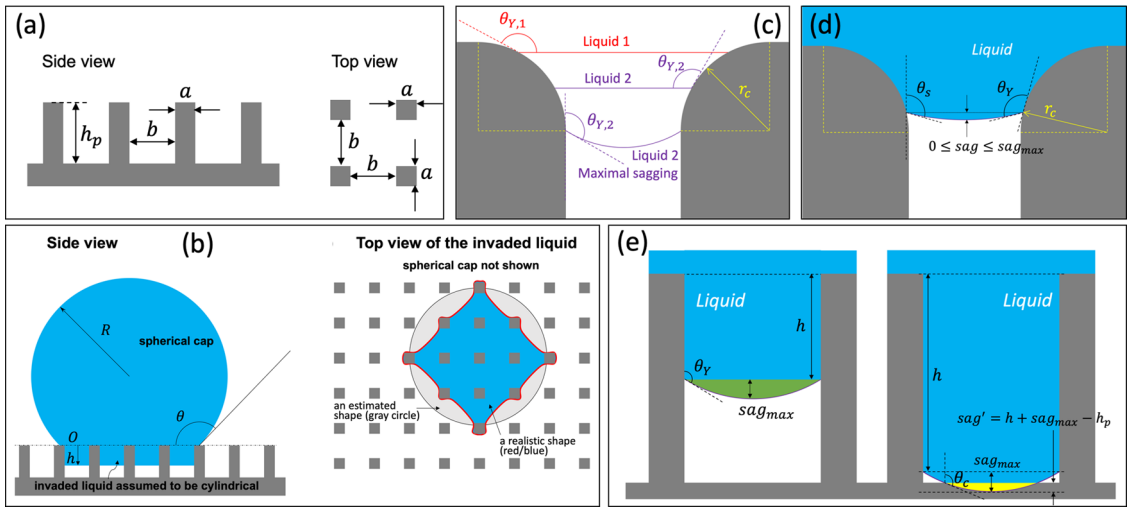

Figure 1. Illustration of the thermodynamic modeling features used or originally proposed in this paper: (a) side and top views of the micropatterned surface made of straight square pillars, where a is the pillar width, b is the pillar spacing, and h_p is the pillar height; (b) side view of a liquid droplet sitting on a micropatterned surface, and the top view of the invaded liquid between the pillars; (c) edge effect is depicted in a magnified view that shows the nanoscale radius of the pillar edge marked as r_c with two liquids of different θ_Y for comparison; (d) unsaturated sagging of Liquid 2 occurring between its flat and maximum sagging locations, where the maximum sagging is shown in (c), and a fake contact angle $\theta_s < \theta_Y$ is used to compute the surface area of the sagged liquid; (e) the maximum sagging with a positive penetration depth for Liquid 2 is depicted on the left, and the sagged liquid touching the substrate bottom is shown on the right, where the contact angle $\theta_c > \theta_Y$ is used on the substrate bottom for simplicity. The green area marks a complete sagging, and the yellow area marks the cutoff region.

states that exist between the Cassie and Wenzel states are associated with the present micropillar patterns as well as additional heterogeneities, such as hierarchical patterns, re-entrant structures, or influential chemical heterogeneity.[37,38] A few assumptions are made to avoid unnecessary complexities involving the metastable states: (1) only ideal micropatterned surfaces consisting of chemically homogeneous straight pillars are studied in this paper (see Figure 1a). (2) The hysteresis on local surfaces of the pillar and substrate is neglected, an assumption that does not nullify the hysteresis due to the micropatterns but only simplifies the local conditions. (3) All sections of the droplet bottom surface penetrate equally into the pillar valleys at the same time.

Justification for these three assumptions are as follows. (1) In this fundamental, mechanistic study, it is convenient to deal with the straight pillars to avoid complex geometric calculations. Straight square pillars are used in this paper; however, the methodology of this paper can be applied to other straight pillar shapes. (2) Neglecting the local hysteresis will eliminate extra energy barriers caused by the nanoscale roughness and/or chemical heterogeneity, and thus, the simplified model will reveal the Gibbs energy and stable states that result from the micropattern alone, excluding the effects of nanoscale geometries. Such surfaces can be called ideal micropatterned substrates. (3) Equal penetration of the droplet bottom surface is frequently met in droplet impact or pressurization experiments. Assuming such a condition in the Gibbs energy study will result in an averaged Wenzel contact angle that is associated with the most stable Wenzel state. Other metastable Wenzel states whose apparent contact angles are less than or greater than this averaged Wenzel contact angle cannot be captured under this assumption.

As illustrated in Figure 1, our simplified model still considers three complicated aspects of wetting on micropatterned surfaces: (i) the liquid volume between pillar valleys is included in the dynamic Gibbs energy calculations (see Figure 1b); (ii) the effect of pillar edges on the droplet sagging is modeled (see Figure 1c,d); and (iii) the smooth transition of the sagged liquid touching the substrate bottom is captured (see Figure 1e). The complete derivation of the modeling process is presented in the following text.

2.1. Droplet Volume above and between Pillars. Most prior Gibbs energy studies neglected the liquid volume between the rough structures,[6−9] which could perfectly derive the original Wenzel and Cassie−Baxter equations analytically. (Note that the Cassie state is not affected by this treatment because no significant liquid volume penetrates into the pillar valleys in the Cassie state.) However, when the liquid volume within the pillar valleys is considered, the minimization of the total Gibbs energy cannot be analytically solved. For instance, the pillar height for many micropatterned surfaces is around h_p = 50 μm, and the liquid volume sinking into the pillar valleys can reach ~0.1% of the liquid volume in the Wenzel state. Although this 0.1% volume is small, its effect on the energy minimization may be non-negligible because the surface areas are changed accordingly (see Section 3 in Supporting Information). The liquid droplet is assumed to be a partial sphere above the pillars, and a cylinder occluded by the pillars, as shown in Figure 1b. Thus, the total liquid volume, V, is

$$V = \frac{4}{3}\pi R^3(2 + \cos\theta)(1 - \cos\theta)^2 + (1 - f)\pi h R^2 \sin^2\theta \tag{3}$$

where R is the droplet radius at a given apparent contact angle, $\theta_{ap} \equiv \theta$, and at a given penetration depth, h ($0 \le h \le h_p$); h_p is the pillar height; $f = a^2/(a + b)^2$; and a and b are pillar width and spacing, respectively. Note that the apparent contact angle is always defined at the pillar top surface. Equation 3 is iteratively solved for given V, θ, and h to compute R. Although a realistic shape of the invaded liquid, as shown in Figure 1b, may attach to the pillars, modeling this kind of realistic conditions is difficult in dynamic calculations of varying θ and h. Thus, the invaded liquid is assumed to be cylindrical in this study. The liquid sagging will be modeled in the following two

DOI: 10.1021/acs.langmuir.9b03002
Langmuir XXXX, XXX, XXX−XXX

Table 1. Equations of Computing the Area of the Liquid−Gas Interface within One Pillar Gap[a]

state	condition	equation	no.
no sagging	sag = 0	$A_{gap} = (a + b)^2 - a^2$	N/A
partial sagging	$0 < sag < sag_{max}$	$A_{gap} = A_{sag}(\theta_s, sag, R_s)$	eq 8
maximum sagging	$sag = sag_{max}$	$A_{gap} = A_{sag}(\theta_Y, sag_{max}, R_Y)$	eq 9
cutaway sagging	$h + sag_{max} > h_p$	$A_{gap} = A_{sag}(\theta_Y, sag_{max}, R_Y) - A_{sag}(\theta_c, sag', R_Y)$	eq 10

[a]Note that $\lim_{sag \to 0} A_{sag}(\theta_s, sag, R_s) = (a + b)^2 - a^2$. The calculation of the liquid−solid interfacial area, A_{ls}, is computed in the same manner of A_{lg} and is presented in Table 2.

subsections with the main purpose of computing the surface area of the sagged liquid. Note that because the volume of the sagged liquid is not significant when compared to the penetrated liquid into the pillar valleys, the volume of the sagged liquid is not considered in eq 3.

Based on these assumptions, the total surface area of the liquid−gas interface is computed as

$$A_{lg} = 2\pi R^2(1 - \cos\theta) + 2\pi Rh \sin\theta + A_{gap}\frac{\pi R^2 \sin^2\theta}{(a + b)^2} \quad (4)$$

where the first term is the area of the spherical cap, the second term is the side area of the invaded liquid, and the third term is the total liquid−gas interfacial area in the pillar gaps. A_{gap} is the liquid−gas interfacial area of one pillar gap, whose value is $A_{gap} = (a + b)^2 - a^2$ if there is no liquid sagging. However, when sagging occurs, A_{gap} will be increased until the maximum sag condition is reached.

2.2. Effect of Pillar Edges. In reality, even the sharpest edge does not possess a perfectly sharp turning point. Therefore, the nanoscale transitional curvature is considered at the pillar top edges. As we zoom into the nanoscale and examine the micropillar's right-angled edges, they will appear to be transitional, curved surfaces instead of pointed edges as shown in Figure 1c. Adapting to the nanoscale curvature, a liquid interface will be flat in equilibrium at a certain location on the nanoscale curved edges, which fulfills the Young's angle on the curved edges. If the flat interface cannot maintain local or global equilibria on the rounded edges, the liquid interface will sag into the pillar valleys. The sagging distance, sag, can be modeled from zero to its maximum value, sag_{max}, the latter of which is computed in terms of the Young's angle, θ_Y, and pillar spacing, b

$$sag_{max} = \frac{b(1 - \sin\theta_Y)}{2|\cos\theta_Y|} \quad (5)$$

The maximum sagging occurs on the vertical wall outside the rounded edges.

This nanoscale sagging transition can be modeled as an increase in sagging, $0 \le sag \le sag_{max}$ (see Figure 1c,d). Because the edge curvature, r_c, is much smaller than the pillar dimensions, the liquid penetration can be neglected before the maximum sagging is reached, i.e., if $sag < sag_{max}$, then $h = 0$. Furthermore, the sagging distance, sag, can be mathematically incorporated into the penetration depth as follows

$$\tilde{h} = \begin{cases} sag - sag_{max}, \text{ if } \tilde{h} < 0 \\ h, \text{ if } \tilde{h} \ge 0 \end{cases} \quad (6)$$

If $\tilde{h} < 0$, then $h = 0$ and $sag = \tilde{h} + sag_{max}$; and if $\tilde{h} \ge 0$, then $h = \tilde{h}$ and $sag = sag_{max}$. Thus, the sagging distance and penetration depth can be unified into one parameter, $\tilde{h}$, whose range is $-sag_{max} \le \tilde{h} \le h_p$. As a result, the modeling and computations will be greatly simplified.

Figure 1d shows an unsaturated sagged interface whose location is between the flat-profile location and maximum sagged location as shown in Figure 1c. The sagging distance, sag, is smaller than the maximum sagging, sag_{max}, and the sagging radii at these two locations are not equal. To compute the surface area of the sagged liquid in the curved transition, A_{sag}, a fake contact angle, $\theta_s < \theta_Y$ (see Figure 1d), is calculated by iteratively solving eq 5 as follows

$$sag = \frac{b(1 - \sin\theta_s)}{2|\cos\theta_s|} \quad (7)$$

A_{sag} is then computed using the Steinmetz shape as an approximation, which is the intersection of two identical cylinders arranged at the right angle

$$A_{sag}(\theta_s, sag, R_s) = 2(2\theta_s - \pi)(a + b)R_s - 8R_s \cdot sag \quad (8)$$

where $R_s = b/(2|\cos\theta_s|)$ is the radius of the sagged liquid that is equal to that of the two cylinders in the Steinmetz shape. In the same manner, the surface area of the maximum sagging is

$$A_{sag,max} = A_{sag}(\theta_Y, sag_{max}, R_Y) \quad (9)$$

where $R_Y = b/(2|\cos\theta_Y|)$ is the maximum sagging radius. Sagging is considered only when the wetting condition is hydrophobic ($\theta_Y > 90°$); when $\theta_Y \le 90°$, sagging will be neglected (hydrophilic cases are not studied in this paper).

2.3. Transition of Touching the Substrate Bottom. As the penetration increases, the sagged liquid will eventually touch the substrate bottom (see Figure 1e). This study models this transition as a part of the Steinmetz surface being cut from the maximum sagged surface, while the sagging radius, R_Y, is kept the same. Thus, the remaining sagged surface is

$$A_{sag,partial} = A_{sag}(\theta_Y, sag_{max}, R_Y) - A_{sag}(\theta_c, sag', R_Y) \quad (10)$$

where $sag' = h + sag_{max} - h_p$ is the vertical distance between the substrate bottom and the virtual location of the maximum liquid sagging and θ_c is a cut angle that plays the role of θ_Y as shown in the left side of Figure 1e for the virtual liquid being cut off by the substrate. Coincidentally, θ_c is also the local contact angle on the bottom surface. To simplify the modeling, θ_Y is not enforced on the substrate bottom, i.e., $\theta_c \ne \theta_Y$ before reaching the full penetration

$$\theta_c = \frac{\pi}{2} + \arccos\left(1 - \frac{sag'}{R_{sag}}\right) \quad (11)$$

2.4. Total Gibbs Energy. The total Gibbs energy, G, is computed as the total surface energy

DOI: 10.1021/acs.langmuir.9b03002
Langmuir XXXX, XXX, XXX−XXX

Table 2. Equations of Computing the Area of the Overall Liquid−Solid Interface

state	condition	formula of A_{ls}
no sagging, partial sagging/max sagging	$h + \text{sag}_{max} < h_p$	$\frac{a^2 + 4ah}{(a+b)^2}\pi R^2 \sin^2\theta$
cutaway sagging	$h + \text{sag}_{max} \geq h_p$ and $h \leq h_p$	$\frac{a^2 + 4ah + 4R_Y(a+b)\lvert\cos\theta_c\rvert - 4R_Y^2\cos^2\theta_c}{(a+b)^2}\pi R^2 \sin^2\theta$
full penetration	$h = h_p$	$\left[1 + \frac{4ah}{(a+b)^2}\right]\pi R^2 \sin^2\theta$

$$G = \sigma_{lg}A_{lg} + \sigma_{ls}A_{ls} + \sigma_{sg}A_{sg} - \sigma_{sg}A_s^{tot} \quad (12)$$

where σ_{lg}, σ_{ls}, and σ_{sg} are the surface tensions of the liquid−gas, liquid−solid, and solid−gas interfaces, respectively; A_{lg}, A_{ls}, and A_{sg} are the corresponding surface areas; and $A_s^{tot} = A_{ls} + A_{sg}$ is the total area of the solid−gas and solid−liquid interfaces. $\sigma_{sg}A_s^{tot}$ is always a constant for a micropatterned substrate. Substituting the Young's equation

$$\sigma_{lg}\cos\theta_Y = \sigma_{sg} - \sigma_{ls} \quad (13)$$

into eq 12, the total Gibbs energy becomes

$$G = \sigma(A_{lg} - A_{ls}\cos\theta_Y) \quad (14)$$

where $\sigma \equiv \sigma_{lg}$ is the liquid−gas surface tension for short.

The liquid−gas interfacial area, A_{lg}, is computed using eq 4, in which A_{gap} is calculated using different equations at different conditions as listed in Table 1.

The formula of A_{ls} at the full penetration condition is a special case of the cutaway sagging condition. The two formulae converge to be the same at the condition of $h = h_p$, and meanwhile, note that $\theta_c = \theta_Y$ when $h = h_p$ according to eqs 5, 7, and 11. The three conditions in Table 2 are mathematically and numerically continuous.

3. CONTINUUM MODELING

In parallel to the thermodynamic modeling, the continuum approach is used to model a realistic wetting process for a water droplet on the same micropatterned surfaces studied in the thermodynamic approach. A Navier−Stokes-type slip boundary model has been developed in the authors' previous works[35,36]

$$\rho\left[\frac{\partial u_s}{\partial t} + u_s\hat{t}_{CL}\cdot\nabla u_s\right] = \beta\nabla_w^2 u_s + [\hat{t}_{CL}\cdot\boldsymbol{\tau}\cdot\hat{n} + \sigma_Y\delta_c]\delta_w \quad (15)$$

where ρ is the fluid density, u_s is the slip velocity of the contact line, t is the time, $\hat{t}_{CL}$ is the tangential direction of the solid surface that is normal to the contact line, ∇_w^2 is the 2D Laplacian operator on the solid surface, β is the friction coefficient of the contact line, τ is the regular fluid stress tensor, $\hat{n}$ is the normal direction of the solid surface, $\sigma_Y = \sigma(\cos\theta_Y - \cos\theta)$ is the unbalanced Young's stress, and δ_c is the delta function of the contact line. The pillars are modeled as physical boundaries on the bottom of the simulation box. The VOF method is used to compute the evolution of the water volume fraction in the internal field, while the slip boundary model is used to march the water fraction on the solid surfaces. The simulation configurations are the same as our previous work,[35] which also presents the grid and time convergence study. Continuum results produced with this setup will be used as a comparison for the thermodynamic calculations. See Supporting Section 1 for simulation configurations and physical parameters. We note that our unique model can capture consistent dynamic contact angles without prescribing the advancing and receding angles.

4. RESULTS AND ANALYSIS

4.1. A 1 μL Water Droplet at a Cassie-Dominated Condition. The Gibbs energy, G, of a 1 μL water droplet on a micropatterned surface, whose parameters are a = 25 μm, h_p = 75 μm, b = 75 μm, and θ_Y = 119°, is computed in a full range of the penetration depths and apparent contact angles. The distribution of G is presented in Figure 2a. To increase the contrast of the distribution, a natural log function, G^*, is presented in Figure 2b

$$G^* = \ln[G - \min(G)] \quad (16)$$

The distribution of G^* clearly shows a Cassie state located at the most bluish spot in Figure 2b, which is the only stable state on this surface. The Cassie contact angle obtained here is exactly the same as that predicted by the Cassie−Baxter equation, which validates the correctness of our modeling on the Cassie state. Meanwhile, both the penetration depth and the sagging distance are found to be zero, which indicate the importance of the pillar edge effect in the Cassie state on the sharp-edged micropatterns. The edge effect favors the

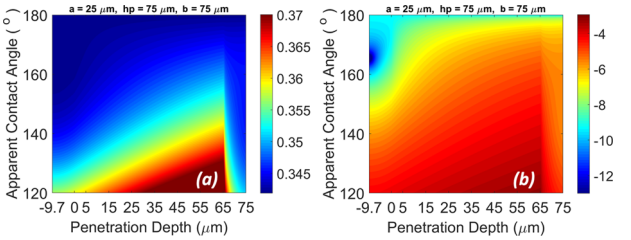

Figure 2. Distribution of the total Gibbs energy at a = 25 μm, h_p=75 μm, and b = 75 μm: (a) the Gibbs energy (unit: μJ), and (b) a natural log function of the Gibbs energy (unitless). The x-axis is the unified penetration depth, $\tilde{h}$, and the y-axis is the apparent contact angle, $\theta \equiv \theta_{ap}$.

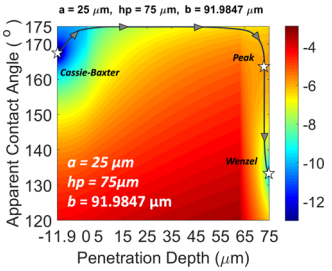

Figure 3. Distribution of G^* at at a = 25 μm, h_p = 75 μm, and b = 91.98 μm: three stars mark the Cassie−Baxter state, Wenzel state, and peak-energy state with an illustrative trajectory of the Cassie-to-Wenzel transition following the normal directions of the energy contours.

DOI: 10.1021/acs.langmuir.9b03002
Langmuir XXXX, XXX, XXX−XXX

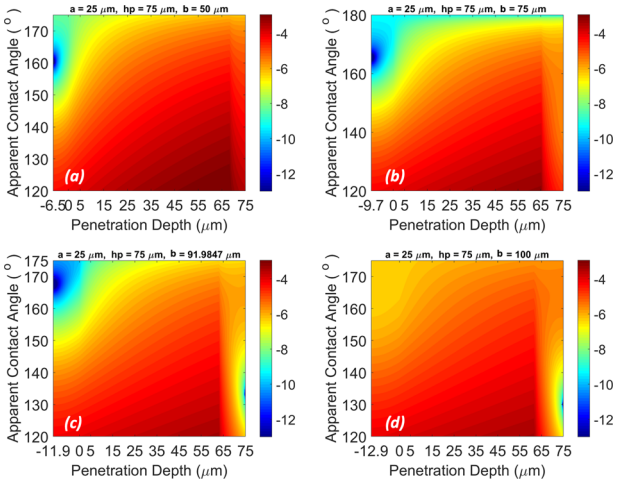

Figure 4. Distribution of G^* at at a = 25 μm, h_p = 75 μm: (a) b = 50 μm, (b) b = 75 μm, (c) b = 91.98 μm, and (d) b = 100 μm.

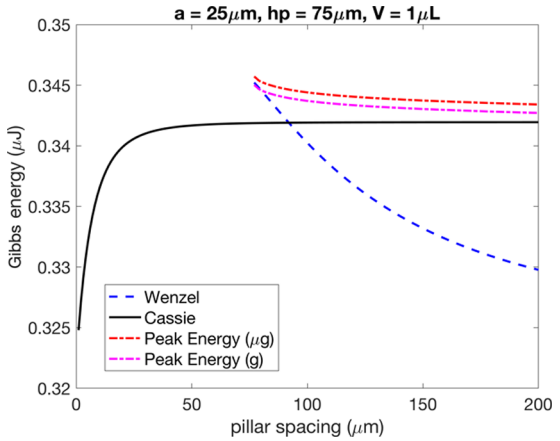

Figure 5. Gibbs energies at a = 25 μm, h_p = 75 μm of the Cassie state (solid line), Wenzel state (dashed line), and two peak-energy states in the microgravity condition (red dash-dotted line) and the terrestrial gravity condition (magenta dash-dotted line).

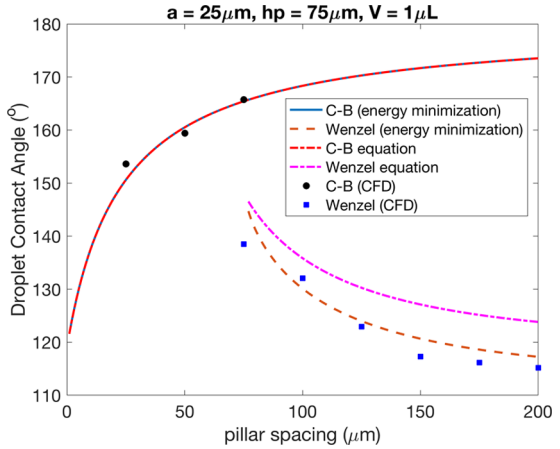

Figure 6. Apparent contact angles at a = 25 μm, h_p = 75 μm of the Cassie state (blue solid line beneath the red solid line), Wenzel state (dashed line) computed using Gibbs energy minimization, the predicted contact angles using the Cassie−Baxter equation (red dash-dotted line), the Wenzel equation (magenta dash-dotted line), and the measured contact angles (discrete points) from the continuum simulations.

formation of a flat interface over the gap of the microstructures in the Cassie-dominated condition. Once the Wenzel state appears and starts to influence wetting, it is possible that a partial liquid sagging on the pillar edges will be favored, which will be investigated in the following subsections. In this case, the maximum sag distance is 9.7 μm, which is reflected in the regions of (1) the edge effect ($\tilde{h} < 0$) and (2) the bottom transition ($\tilde{h} > h_p - \mathrm{sag}_{max}$). Although there is no Wenzel state shown in Figure 2b, the color contour of G^* near the substrate bottom indicates that the Wenzel state is likely to form near (θ = 145°, $\tilde{h} = h_p$) if the pillar spacing is increased.

4.2. Simultaneous Cassie and Wenzel States with the Same Gibbs Energy. For micropatterned surfaces with the same pillar width and height, the Wenzel state will appear for larger pillar spacings and become increasingly dominant as the gap widens. This study shows that for micropatterns with a = 25 μm and h_p= 75 μm, the Wenzel state appears at b = 77 μm. When b = 91.98 μm, the Gibbs energy of the Wenzel state becomes the same as that of the Cassie state, whose distribution of G^* is presented in Figure 3. Note that the blue region of the Cassie state is larger than that of the Wenzel state, which indicates that, although both states have an equal Gibbs energy, the Cassie state has more influence than the Wenzel state. An illustrative trajectory of the Cassie-to-Wenzel transition is also drawn in Figure 3 as a curve following the normal directions of the energy contours. Starting from the Cassie state, the Gibbs energy increases until reaching a peak-energy state, and finally, it decreases until reaching the Wenzel state. The energy difference between the Cassie and peak-energy states is the energy barrier of the Cassie-to-Wenzel transition, while the energy difference between the Wenzel and peak-energy states is the energy barrier of the Wenzel-to-Cassie transition. The two energy barriers are equal in magnitude (2.7 nJ) in this case. But because the bluish area is larger in the Cassie state, a 1 μL water droplet will more likely stay in the Cassie state if the system is perturbed. Otherwise, the droplet state depends on the deposition method and manipulation history. Note that this study neglects the local hysteresis on the substrate surfaces, so the computed energy barriers will be smaller than in reality. Nevertheless, this study will reveal states and energy distributions due to the micropatterns, which are important to understand the wetting phenomena for this scale of roughness.

4.3. Whole Picture of Wetting on Substrates with the Same Pillar at Different Spacings. To explore the changes of the wetting states at different pillar spacings, the Gibbs energy has been calculated for a series of pillar spacings, from 1 to 200 μm, while maintaining the same pillar width and height (a = 25 μm, h_p = 75 μm). The distributions of G^* at four pillar spacings, b = 50, 75, 91.98, and 100 μm, are presented in Figure 4 (note that two of them had been previously presented in Sections 4.1−4.2). At b = 50 μm, it is a Cassie wetting state with zero penetration, zero sagging, and no coexisting Wenzel state. At b = 75 μm, it is still a Cassie wetting state with zero penetration, zero sagging, and no Wenzel state; however, a dip in the Wenzel region is formed and becomes more dominant as the spacing increases. At b = 91.98 μm, it is a mixed wetting condition with competing Cassie and Wenzel states: the Cassie state has zero penetration and zero sagging, while the Wenzel state holds full penetration. At b = 100 μm, the mixed wetting condition is still present but the Wenzel state is now dominant: the Wenzel state has a lower Gibbs energy than the Cassie

DOI: 10.1021/acs.langmuir.9b03002
Langmuir XXXX, XXX, XXX−XXX

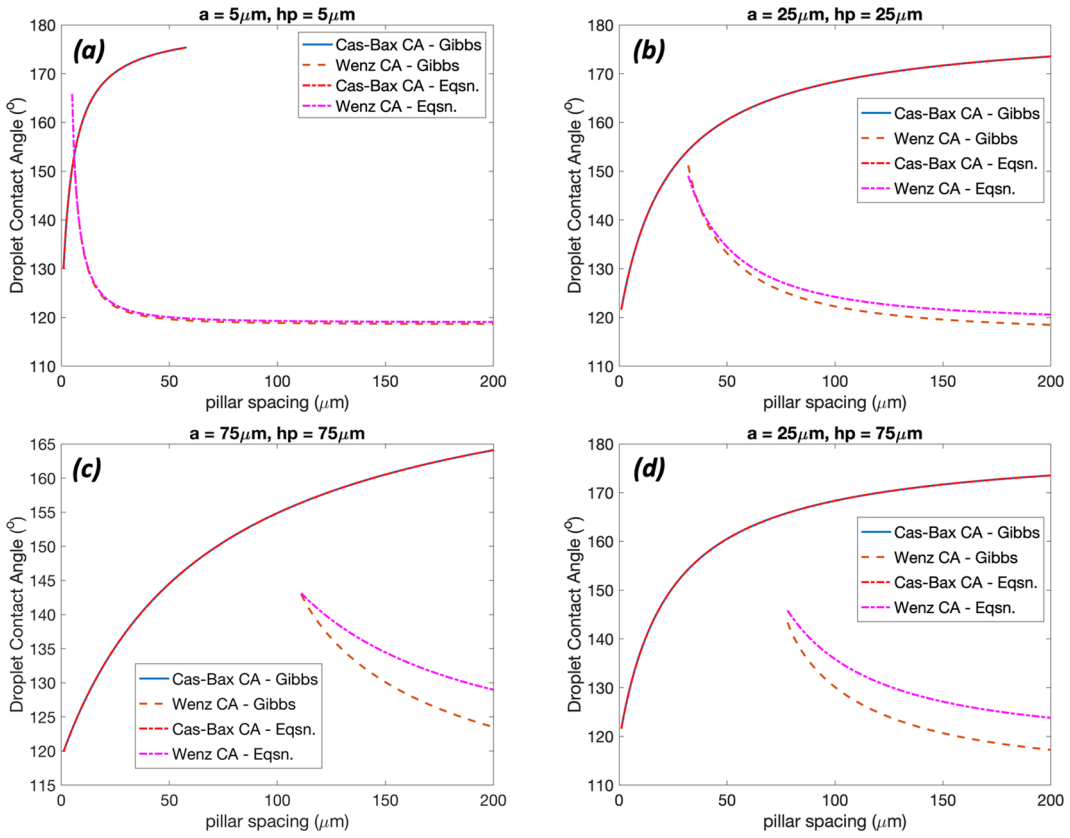

Figure 7. Apparent contact angles at (a) a = 5 μm, h_p = 5 μm; (b) a = 25 μm, h_p = 25 μm; (c) a = 75 μm, h_p = 75 μm; and (d) a = 25 μm, h_p = 75 μm.

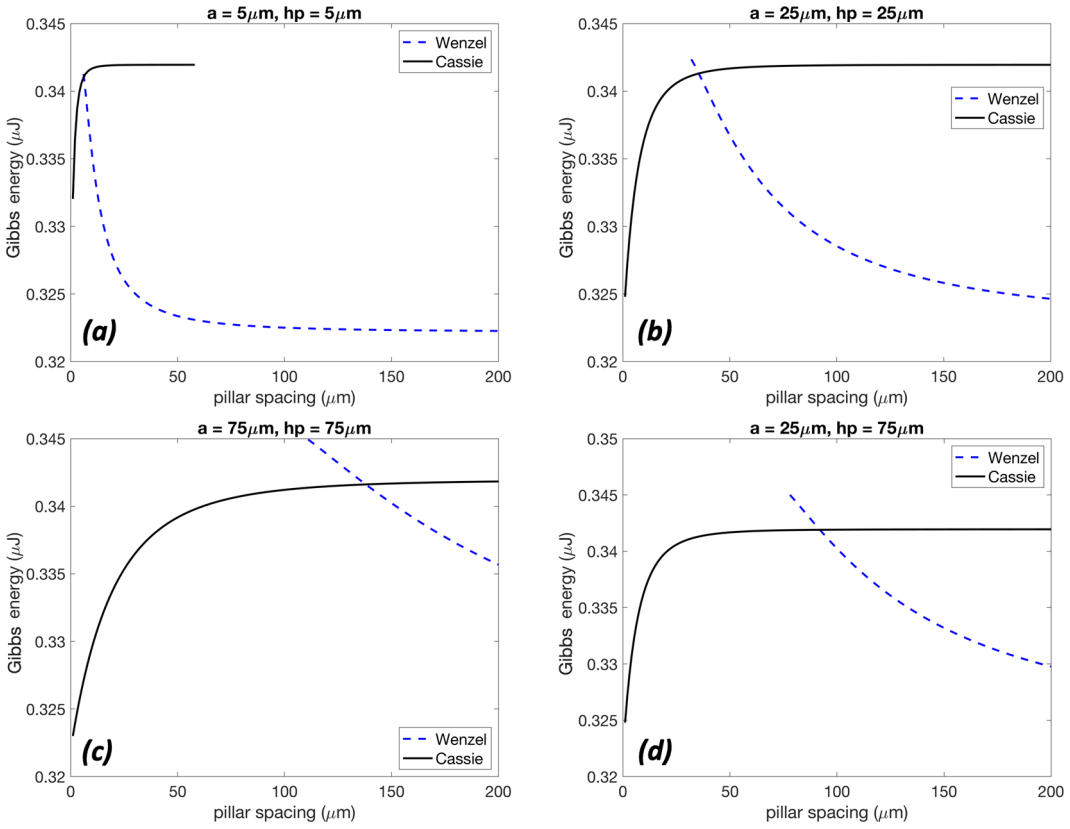

Figure 8. Gibbs energies of the Cassie and Wenzel states at (a) a = 5 μm, h_p = 5 μm; (b) a = 25 μm, h_p = 25 μm; (c) a = 75 μm, h_p = 75 μm; and (d) a = 25 μm, h_p = 75 μm.

DOI: 10.1021/acs.langmuir.9b03002
Langmuir XXXX, XXX, XXX−XXX

state; meanwhile, the Cassie state remains at zero penetration and zero sagging as in the Cassie-dominated conditions.

Figure 5 shows the Gibbs energies of the Cassie state, the Wenzel state, and the peak-energy state at pillar spacings of b = 1−200 μm based on the same Gibbs energy minimization as shown in Figure 4. At small spacings (b < 30 μm), the Cassie-state energy quickly increases with the pillar spacing, and after b = 30 μm, the increasing rate reduces. At b = 77 μm, the Wenzel state appears with a higher Gibbs energy (G_W = 0.3452 μJ) than the Cassie state (G_{CB} = 0.3419 μJ) for this same spacing. Beyond this point, the Wenzel-state energy decreases with spacing, and the two states converge at b = 91.98 μm. For b > 91.98 μm, the Wenzel state is dominant, and the energy difference grows rapidly with spacing because the liquid−gas interface cannot be supported on top of the pillars as the pillar spacing increases.

The peak energy presented as the red dash-dotted curve in Figure 5 marks the energy barriers between the Cassie and Wenzel states without the consideration of gravity. The peak energy is always higher than the two stable states, which means there is always an energy barrier between the Cassie and Wenzel states. When the Wenzel-state energy becomes much smaller than the Cassie state, the energy barrier of the Cassie-to-Wenzel transition is significantly lower than that of the Wenzel-to-Cassie transition. Thus, the Cassie-to-Wenzel transition can be termed as irreversible because it is easy to transition from Cassie to Wenzel but difficult to go back.

In general, the energy barrier of the Cassie-to-Wenzel transition is not large (2.2−3.4 nJ), which indicates an easy transition from the higher-energy state to the lower-energy state. When gravity is considered, the energy barrier is further lowered with the assistance of the gravitational potential energy shown as the magenta dash-dotted curve in Figure 5.

From the energy minimization results, the corresponding apparent contact angles can be found. These are presented in Figure 6 together with two data sets: (1) the theoretical predictions using the Cassie−Baxter and Wenzel equations and (2) the measured angles from the continuum simulations. The Cassie contact angle calculated from energy minimization is the same as the results of the Cassie−Baxter equation at all spacings. The continuum simulations match well with these angles in the Cassie state. However, in the Wenzel state, there is a deviation of more than 5° between the results of energy minimization and those of the Wenzel equation. This phenomenon can be referred to as the Wenzel deviation. The deviation is small at b = 77 μm and increases with spacing. The results of the continuum simulations differ from the Wenzel equation and confirm this Wenzel deviation. See Supporting Section 2 and Videos S1−S6 for the simulation results.

4.4. Elucidating the Wenzel Deviation. Is the Wenzel deviation correct? Do we expect to have the Wenzel deviation? Why is the Cassie state not deviated from the Cassie−Baxter equation? To answer these questions, one needs to understand the assumptions held when deriving the Cassie−Baxter and Wenzel equations. The main premise set for deriving both equations is that the droplet size is much greater than the average size of the rough structures so that the liquid volume and liquid−gas interfacial area between the rough structures are negligible. As the roughness size increases to be large enough, the deviation of the Wenzel equation from reality is actually expected (see Section 3 in Supporting Information). However, the Cassie state is expected to have no deviation on the straight-pillared surfaces because there is no liquid penetration or sagging between the rough structures (except for the cases of curved micropatterns, when the Cassie state is stabilized at a relatively large partial penetration).

As discussed above, the Wenzel deviation is expected. This deviation is confirmed using continuum simulations. But would we validate this deviation through the method of energy minimization? The deviation can be tested by making the same comparisons in Figure 6 using smaller pillar sizes. Figure 7 presents the apparent contact angles of four pillar sizes: (a) a = 5 μm, h_p = 5 μm, (b) a = 25 μm, h_p = 25 μm, (c) a = 75 μm, h_p = 75 μm, and (d) a = 25 μm, h_p = 75 μm (the last of which is the representative case presented in Section 4.3). At a = 5 μm and h_p = 5 μm, the Wenzel deviation is less than 0.5°. The deviation increases with the pillar height as shown in Figure 7a,b,d. Comparing Figure 7c,d, one will find that the increase in the pillar width only delays the occurrence of the Wenzel state at a larger spacing; however, between the two pillar widths, a = 25 μm and a = 75 μm, the maximum Wenzel deviation does not change, indicating that the pillar height determines the maximum deviation. The Gibbs energies of the pillar dimension series just described are presented in Figure 8.

5. CONCLUSIONS

In this paper, a sophisticated Gibbs energy model has been developed to study wetting phenomena on micropatterned substrates made of straight micropillars, and the continuum simulations developed in our previous studies have been used to compare with the Gibbs energy model. As the micropillar height increases, incorporating the liquid volume and liquid−gas interfacial area into the Gibbs energy analysis becomes important. In addition, this paper incorporated the liquid sagging transition in the Cassie state as well as in the Wenzel state. Based on the unique model developed in this paper, the energy minimization calculations of a 1 μL water droplet on a series of micropatterned surfaces have revealed that (1) the Cassie state favors zero penetration and zero sagging on the straight pillared surfaces, (2) the energy barriers between the Cassie and Wenzel states are small, and (3) more importantly, when the pillar height is large, the real-world Wenzel states deviate from the predictions of the Wenzel equation, e.g., more than 6° when h_p = 75 μm. Note that because the height of 75 μm or greater is frequently used when developing engineered surfaces, the Wenzel equation will not be able to accurately predict the Wenzel contact angle for a wide range of applications. Therefore, the model developed in this paper is needed to predict the Wenzel state for these micropatterns.

■ ASSOCIATED CONTENT

Supporting Information

The Supporting Information is available free of charge on the ACS Publications website at DOI: 10.1021/acs.langmuir.9b03002.

Simulation configurations and physical parameters; detailed comparisons between Gibbs energy calculations and CFD simulations; theoretical explanation of the Wenzel deviation; Screenshots of Supplementary Videos S1−S6; Table S1: Comparison of Gibbs energy calculations and numerical simulations; Table S2: List of the supporting videos made from the continuum simulations (PDF)

DOI: 10.1021/acs.langmuir.9b03002
Langmuir XXXX, XXX, XXX−XXX

Videos of the continuum simulations: Video S1: CB-50um.mp4; Video S2: CB-75um.mp4; Video S3: WZ-75um.mp4; Video S4: WZ-100um.mp4; Video S5: CB-3Cases.mp4; Video S6: WZ-3Cases.mp4 (MP4) (MP4) (MP4) (MP4) (MP4) (MP4)

AUTHOR INFORMATION

Corresponding Author

*E-mail: phe@lamar.edu.

ORCID

Ping He: 0000-0002-2671-8657

Notes

The authors declare no competing financial interest.

ACKNOWLEDGMENTS

We acknowledge the Center for Innovation, Commercialization and Entrepreneurship (CICE), and the Center for Advances in Port Management at Lamar University for grant awards in 2019. We acknowledge the Office of Undergraduate Research (OUR) at LU for supporting Chae Rohrs with the prestigious 2018/19 OUR Grant Award. We greatly appreciate Paul Latiolais and Dr. Hsing-Wei Chu for discussions and encouragement. We acknowledge the Texas Advanced Computing Center (TACC) at UT Austin for funding computational hours (Grant no. G-819854). We thank the IT Infrastructure Department at LU for hosting our HPC cluster, and especially thank Chad Smith for helping us with HPC maintenance.

REFERENCES

(1) Wenzel, R. N. Resistance of solid surfaces to wetting by water. *Ind. Eng. Chem.* **1936**, *28*, 988−994.

(2) Cassie, A. B. D.; Baxter, S. Wettability of porous surfaces. *Trans. Faraday Soc.* **1944**, *40*, 546−550.

(3) Kawai, A.; Nagata, H. Wetting Behavior of Liquid on Geometrical Rough-Surface Formed by Photolithography. *Jpn. J. Appl. Phys., Part 2* **1994**, *33*, L1283−L1285.

(4) Bico, J.; Marzolin, C.; Quere, D. Pearl drops. *Europhys. Lett.* **1999**, *47*, 220−226.

(5) Johnson, R. E., Dettre, R. H. Contact Angle Hysteresis. *Contact Angle, Wettability, and Adhesion*; American Chemical Society, 1964; Vol. *43*, pp 112−135.

(6) Patankar, N. A. On the modeling of hydrophobic contact angles on rough surfaces. *Langmuir* **2003**, *19*, 1249−1253.

(7) He, B.; Patankar, N. A.; Lee, J. Multiple equilibrium droplet shapes and design criterion for rough hydrophobic surfaces. *Langmuir* **2003**, *19*, 4999−5003.

(8) Marmur, A. Wetting on hydrophobic rough surfaces: To be heterogeneous or not to be? *Langmuir* **2003**, *19*, 8343−8348.

(9) Patankar, N. A. Transition between superhydrophobic states on rough surfaces. *Langmuir* **2004**, *20*, 7097−7102.

(10) Tuteja, A.; Choi, W.; Mabry, J. M.; McKinley, G. H.; Cohen, R. E. Robust omniphobic surfaces. *Proc. Natl. Acad. Sci. USA* **2008**, *105*, 18200−18205.

(11) Whyman, G.; Bormashenko, E. Wetting Transitions on Rough Substrates: General Considerations. *J. Adhes. Sci. Technol.* **2012**, *26*, 207−220.

(12) Patankar, N. A. Consolidation of Hydrophobic Transition Criteria by Using an Approximate Energy Minimization Approach. *Langmuir* **2010**, *26*, 8941−8945.

(13) Pashos, G.; Kokkoris, G.; Boudouvis, A. G. Minimum Energy Paths of Wetting Transitions on Grooved Surfaces. *Langmuir* **2015**, *31*, 3059−3068.

(14) Guo, H. Y.; Li, B.; Feng, X. Q. Stability of Cassie-Baxter wetting states on microstructured surfaces. *Phys. Rev. E* **2016**, *94*, No. 042801.

(15) Sarkar, A.; Kietzig, A. M. General equation of wettability: A tool to calculate the contact angle for a rough surface. *Chem. Phys. Lett.* **2013**, *574*, 106−111.

(16) Bormashenko, E. Progress in understanding wetting transitions on rough surfaces. *Adv. Colloid Interface Sci.* **2015**, *222*, 92−103.

(17) Whyman, G.; Bormashenko, E. How to Make the Cassie Wetting State Stable? *Langmuir* **2011**, *27*, 8171−8176.

(18) Liu, T. Q.; Li, Y. J.; Li, X. Q.; Sun, W. Theoretical analysis of droplet transition from Cassie to Wenzel state. *Chin. Phys. B* **2015**, *24*, No. 116801.

(19) Liu, T. Q.; Li, Y. J.; Li, X. Q.; Sun, W. Mechanism Study on Transition of Cassie Droplets to Wenzel State after Meniscus Touching Substrate of Pillars. *J. Phys. Chem. C* **2017**, *121*, 9802−9814.

(20) Dong, J.; Jin, Y. L.; Dong, H.; Sun, L. Numerical Calculation Method of Apparent Contact Angles on Heterogeneous Double-Roughness Surfaces. *Langmuir* **2017**, *33*, 10411−10418.

(21) Zhu, L.; Feng, Y. Y.; Ye, X. Y.; Zhou, Z. Y. Tuning wettability and getting superhydrophobic surface by controlling surface roughness with well-designed microstructures. *Sens. Actuators, A* **2006**, *130*−*131*, 595−600.

(22) Barbieri, L.; Wagner, E.; Hoffmann, P. Water wetting transition parameters of perfluorinated substrates with periodically distributed flat-top microscale obstacles. *Langmuir* **2007**, *23*, 1723−1734.

(23) Erbil, H. Y.; Cansoy, C. E. Range of Applicability of the Wenzel and Cassie-Baxter Equations for Superhydrophobic Surfaces. *Langmuir* **2009**, *25*, 14135−14145.

(24) Bormashenko, E.; Bormashenko, Y.; Stein, T.; Whyman, G.; Pogreb, R.; et al. Environmental scanning electron microscopy study of the fine structure of the triple line and Cassie-Wenzel wetting transition for sessile drops deposited on rough polymer substrates. *Langmuir* **2007**, *23*, 4378−4382.

(25) Noscinovsky, M.; Bhushan, B. Patterned nonadhesive surfaces: Superhydrophobicity and wetting regime transitions. *Langmuir* **2008**, *24*, 1525−1533.

(26) Wang, G.; Jia, Z. H.; Yang, H. N. Stability of a water droplet on micropillared hydrophobic surfaces. *Colloid Polym. Sci.* **2016**, *294*, 851−858.

(27) Pinchasik, B.-E.; Wang, H. Q.; Mohwald, H.; Asanuma, H. Fully Reversible Transition between Cassie and Wenzel States via Acoustic Waves. *Adv. Mater. Interfaces* **2016**, *3*, No. 1600722.

(28) Jung, Y. C.; Bhushan, B. Wetting transition of water droplets on superhydrophobic patterned surfaces. *Scr. Mater.* **2007**, *57*, 1057−1060.

(29) Jung, Y. C.; Bhushan, B. Dynamic Effects Induced Transition of Droplets on Biomimetic Superhydrophobic Surfaces. *Langmuir* **2009**, *25*, 9208−9218.

(30) Murakami, D.; Jinnai, H.; Takahara, A. Wetting Transition from the Cassie-Baxter State to the Wenzel State on Textured Polymer Surfaces. *Langmuir* **2014**, *30*, 2061−2067.

(31) Koishi, T.; Yasuoka, K.; Fujikawa, S.; Ebisuzaki, T.; Zeng, X. C. Coexistence and transition between Cassie and Wenzel state on pillared hydrophobic surface. *Proc. Natl. Acad. Sci. USA* **2009**, *106*, 8435−8440.

(32) Gong, W.; Zu, Y. Q.; Chen, S.; Yan, Y. Y. Wetting transition energy curves for a droplet on a square-post patterned surface. *Sci. Bull.* **2017**, *62*, 136−142.

(33) Lee, J. S.; Moon, J. Y.; Lee, J. S. Study of transporting of droplets on heterogeneous surface structure using the lattice Boltzmann approach. *Appl. Therm. Eng.* **2014**, *72*, 104−113.

(34) Zhang, W.; Zhang, R. R.; Jiang, C. G.; Wu, C. W. Effect of pillar height on the wettability of micro-textured surface: Volume-of-fluid simulations. *Int. J. Adhes. Adhes.* **2017**, *74*, 64−69.

(35) Azimi, A.; He, P.; Rohrs, C.; Yao, C. W. Developing a novel continuum model of static and dynamic contact angles in a case study of a water droplet on micro-patterned hybrid substrates. *MRS Commun.* **2018**, *8*, 1445−1454.

(36) He, P.; Yao, C.-W. Simulating contact angle hysteresis using pseudo-line tensions. *MRS Commun.* **2019**, *9*, 1060−1066.

DOI: 10.1021/acs.langmuir.9b03002
Langmuir XXXX, XXX, XXX−XXX

(37) Long, J.; Hyder, M. N.; Huang, R. Y. M.; Chen, P. Thermodynamic modeling of contact angles on rough, heterogeneous surfaces. *Adv. Colloid Interface Sci.* **2005**, *118*, 173−190.
(38) Marmur, A.; Bittoun, E. When Wenzel and Cassie Are Right: Reconciling Local and Global Considerations. *Langmuir* **2009**, *25*, 1277−1281.

DOI: 10.1021/acs.langmuir.9b03002
Langmuir XXXX, XXX, XXX−XXX